Imaging Through Unknown Walls Using Different Standoff Distances

Genyuan Wang, *Member, IEEE*, and Moeness G. Amin, *Fellow, IEEE*

***Abstract*—In through-the-wall imaging, errors in wall parameters cause targets to be imaged away from their true positions. The displacement in target locations depend on the accuracy of the estimates of the wall parameters as well as the target position relative to the antenna array. A technique using two or more standoff distances of the imaging system from the wall is proposed for application under wall parameter ambiguities. Two different imaging schemes can then be applied to correct for errors in wall characteristics. The first scheme relies on forming target displacement trajectories, each corresponding to a different standoff distance, and assuming different values of wall thickness and dielectric constant. The target position is then determined as the trajectories crossover point. In the second scheme, an image sequence is generated. Each specific image in this sequence is obtained by summing those corresponding to different standoff distances, but with the same assumed wall parameters. An imaging-focusing metric can then be adopted to determine the target position. The paper analyzes the above two schemes and provides extensive simulation examples demonstrating their effectiveness.**

***Index Terms*—Autofocusing, radar imaging, through-the-wall, wideband beamforming.**

I. Introduction

THROUGH-THE-WALL radar imaging (TWRI) is an emerging technology that addresses a number of civilian problems and has a dual-use with obvious military applications as well. TWRI is a complex and difficult problem that requires cross-disciplinary research. Fundamentally, it is a hybrid between two main areas, statistical signal, radar, and array processing, on one hand, and antennas and electromagnetics, on the other. There are many challenges facing TWRI system development, namely, the system should be reliable, portable, light weight and small size and have both short acquisition time and setup time. It is important for the system performance to be robust to ambiguities and inaccuracies in wall parameters and to the presence of nonuniform walls, multiple walls, and operator motion. Ultimately, the system should have high-range and cross-range resolutions, which are application specific. Finally, the TWRI system must be able to detect and classify motions in a populated scene and in the presence of heavy clutter, which may include interior back and side walls, water pipes, electrical cords, and various types of furniture items.

There are two different approaches to TRWI. The first approach is coherent imaging that requires wideband beamforming to be applied, using transmitter and receiver antenna arrays [1]–[11]. The other is the noncoherent approach that involves several, more simplified and stand-alone radar units. In this case, imaging is performed based on the trilateration technique [12]–[17]. In this paper, we focus on the coherent imaging approach. There are several studies on the coherent TWRI to detect stationary and moving target behind the walls with known wall characteristics, such as dielectric constant [1]–[11]. In practical situations, however, the wall parameters are not exactly known. The errors in wall parameters impact the imaged target position as well as the target spread and intensity profile. A TWRI technique that provides correct target location without the knowledge of the wall parameters was proposed in [18]. The technique in [18] requires data to be acquired using at least two different array placement positions against the wall. At each position, imaging is performed for different assumed values of wall parameters. The displacements in target position due to incorrect wall parameter values form a trajectory, which traces the highest peak of the target image as its shifts. The trajectories for different array positions, or structures, are shown to intersect at the true target position. The application of the scheme proposed in [18], however, may be limited in practice. Safety reasons may prohibit the system operator from reaching the wall.

Inspired by the work in [18], we introduce in this paper two new approaches for imaging of point targets under wall parameter ambiguities. In both schemes, imaging is performed at least at two standoff distances. At each standoff distance, the array may be arbitrarily placed. These schemes include the approach in [18] as a special case, where the array is only placed against the wall. In the first proposed approach, for each standoff distance, several images are obtained using different assumed wall characteristics. The extent of the shift of the target image from its true position depends on the error between the assumed and exact wall parameters. The target displacement trajectory is then constructed by connecting the peak values of its images. The intersection of the trajectories corresponding to different standoff distances indicates the target position.

The above approach is effective at short distances from the wall. We note that, unlike the approach in [18] in which the imaging system only moves parallel to the wall, different standoff distances from the wall can generate images with significantly different angle resolutions. The image of a target from a long standoff distance occupies several image pixels in

Manuscript received June 20, 2005; revised October 24, 2005. The associate editor coordinating the review of this manuscript and approving it for publication was Dr. Petr Tichavsky. This work is supported by DARPA under grant MDA972-02-1-0022 and in part by ONR grant N00014-98-1-0176. The content of the information does not necessarily reflect the position or the policy of the Government, and no official endorsement should be inferred.

The authors are with Radar Imaging Laboratory, Center for Advanced Communications, Villanova University, Villanova, PA 19085 USA (e-mail: genyuan.wang@villanova.edu; moeness.amin@villanova.edu).

Digital Object Identifier 10.1109/TSP.2006.879325

both angle and range, especially for targets with large incident angle. To overcome image dispersion, we propose a second approach in which we use the effects of both target displacement and blurriness. A composite image sequence is generated with different wall parameters using two or more standoff distances. Each specific element in the image sequence is obtained, for given wall parameter values, by summing the images generated at the two array positions. Since targets are imaged in their true positions with least blurriness when correct wall parameters are used, an image focusing metric may be applied to determine the image corresponding to proper wall thickness and dielectric constant. In this paper, we use the entropy measure [19], [20] and show its effectiveness in locating the target behind unknown walls.

The organization of the paper is as follows. In Section II, we provide the fundamental equations of wideband TRWI from a standoff distance. The effect of wall parameter ambiguities on target displacement is discussed in Section III. In Section IV, a target location estimation approach using of two or more standoff distances is presented. In Section V, we propose a general implementation of TWRI and target location estimation using two or more array positions at long standoff distances. The conclusion is provided in Section VI.

II. Wideband Beamforming

The wideband beamforming for imaging through the wall was presented in [9], [18], for system antennas placed against the wall. Below, we discuss the general case for arbitrary standoff distance. An M-element transmit and an N-element receive system is used for imaging. The region to be imaged is located along the positive z axis. The mth transmitter, located at $\mathbf{x}_{t_m} = (x_{t_m}, z_{t_m})$, illuminates the scene with the wideband signal $s(t)$. The reflection by any target located in the region being imaged is collected at the nth receiver located at $\mathbf{x}_{r_n} = (x_{r_n}, z_{r_n})$. For a single point target located at $\mathbf{x}_p = (x_p, z_p)$, the output of the nth receiver is given by

$$y_{mn}(\mathbf{x}_p) = a(\mathbf{x}_p)s(t - \tau_{p,mn}) \tag{1}$$

where $a(\mathbf{x}_p)$ is the complex reflectivity of the point target. The propagation delay, $\tau_{p,mn}$, encountered by the signal as it travels from the mth transmitter to the target located at $\mathbf{x}_p$, and back to the nth receiver, is given by

$$\tau_{p,mn} = \frac{r_{m,p} + r_{n,p}}{c} + \frac{l_{m,p} + l_{n,p}}{v} \tag{2}$$

where c and v are the propagation speeds in the air and in the wall, respectively. The variables $r_{m,p}$ and $r_{n,p}$ ($l_{m,p}$ and $l_{n,p}$), respectively, represent the traveling distances of the wave in the air (wall) from the mth transmitter to the target p and from the target to the nth receiver. These parameters are depicted in Fig. 1.

The region of interest is divided into a finite number of pixels in range and angle. The complex composite signal corresponding to the image of the pixel located at $\mathbf{x}_q$ (at range R_q in the direction θ_q) is obtained by applying time delays and weights to the data at the N receivers, and summing the results. The block diagram of the imaging system is shown in Fig. 2. For a single target case, the system output is given by [9]

$$b_q(t) = \sum_{m=1}^{M}\sum_{n=1}^{N} w_{t_m} w_{r_n} a(\mathbf{x}_p) s(t - \tau_{p,mn} + \tau_{q,mn}) \tag{3}$$

where w_{r_n} and w_{t_m} are the weights applied to the output of the nth receiver and the component signal obtained using the mth transmitter. The focusing delay $\tau_{q,mn}$ is applied to the output of the nth receiver when the transmitter is at the mth location. This delay, which is given by

$$\tau_{q,mn} = \frac{r_{m,q} + r_{n,q}}{c} + \frac{l_{m,q} + l_{n,q}}{v} \tag{4}$$

synchronizes the arrivals at different receive locations for the same pixel, and as such allows coherent imaging. The complex amplitude image value for the pixel located at $\mathbf{x}_q$ is obtained by passing the signal $b_q(t)$ through a filter $h(t) = s^*(-t)$, which is matched to the transmitted pulse, and sampling the output of the filter at time $t = 0$,

$$I(\mathbf{x}_q) = (b_q(t) * h(t))\,|_{t=0}. \tag{5}$$

The process described by (3) and (5) is performed for all pixels in the region of interest to generate the composite image of the scene. The general case of multiple targets can be obtained by superposition of target reflections.

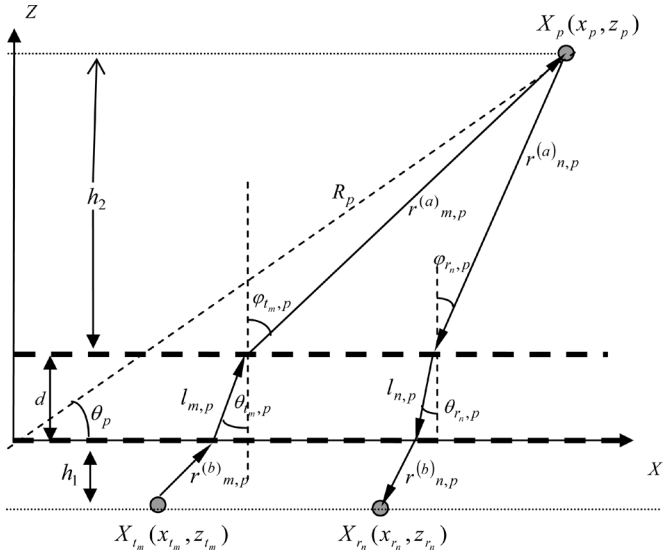

Fig. 1. Geometry for computing the distances on transmit and receive arrays.

III. Target Image Displacement

Errors in wall thickness and dielectric constant impact the traveling time both inside and outside the wall, and subsequently, lead to errors in the applied focusing delays for coherent imaging, given by (4). Using estimates, denoted by "$\sim$", rather than true values of the wall parameters, (4) changes to

$$\widetilde{\tau}_{q,mn} = \frac{\widetilde{r}_{m,q} + \widetilde{r}_{n,q}}{c} + \frac{\widetilde{l}_{m,q} + \widetilde{l}_{n,q}}{\widetilde{v}} \tag{6}$$

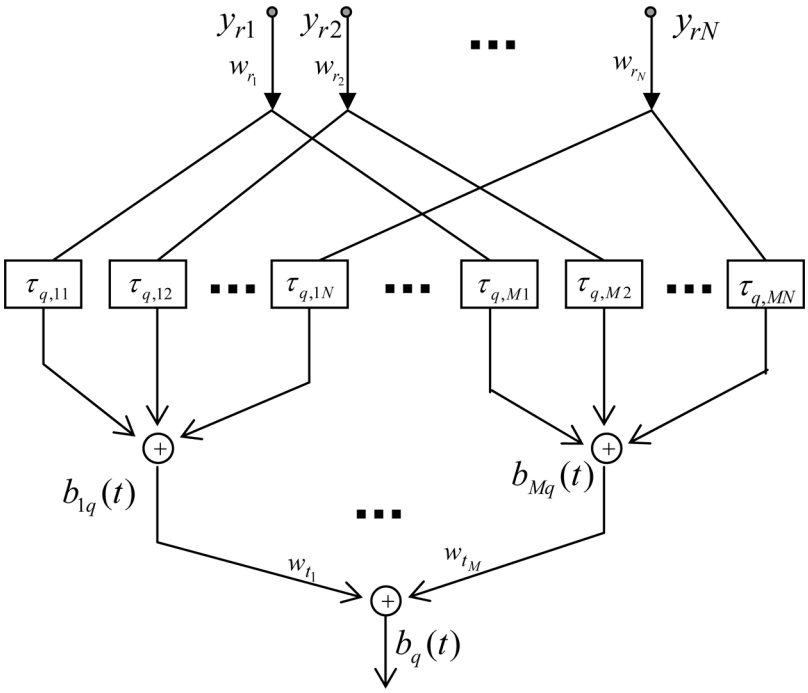

Fig. 2. Block diagram of the post-data-acquisition beamformer.

where $\tilde{v} = c/\sqrt{\varepsilon_e}$ is the estimated propagation speed through the wall. Due to errors in propagation speed, $\tilde{\tau}_{q,mn} \neq \tau_{q,mn}$. A shift in target position due to focusing delay errors will require $\tilde{\tau}_{q,mn} = \tau_{p,mn}, \forall m, n$, i.e., a new set of focusing delays in the presence of wall errors must equal the target propagation delays, given by (2).

A. Effect of Wall Thickness Errors

If the assumed wall thickness is $d_e = d + \Delta d$, and the dielectric constant is known, then the focusing delay for the target at the pth image pixel from the mth transmit antenna to the nth receive antenna is

$$\tilde{\tau}_{p,mn,d} = \tau_{p,mn} + \Delta\tau_{p,mn,d} \tag{7}$$

(2), with $q = p$, can be rewritten as

$$\tau_{p,mn} = \frac{h}{c\cos(\varphi_{t_m,p})} + \frac{h}{c\cos(\varphi_{r_n,p})} + \frac{\sqrt{\varepsilon}d}{c\cos(\theta_{t_m,p})} + \frac{\sqrt{\varepsilon}d}{c\cos(\theta_{r_n,p})} \tag{8}$$

where $h = h_1 + h_2 = z_p - z_{t_m} - d$. The parameters h_1 and h_2 are, as shown in Fig. 1, the distances of the wall to the transmit antenna and the target, respectively. The change in focusing delay due to the error Δd is

$$\Delta\tau_{p,mn,d} = \frac{\Delta d}{c}\left(\frac{\sin(\varphi_{t_m,p} - \theta_{t_m,p})}{\sin(\theta_{t_m,p})} + \frac{\sin(\varphi_{r_n,p} - \theta_{r_n,p})}{\sin(\theta_{r_n,p})}\right). \tag{9}$$

The derivation of (9) is given in Appendix A. It is clear from the above equation that the change in the focusing delay is a linear function of Δd and is a nonlinear function of the incident angles. This shows that the change in the focusing delay is generally antenna dependent. If the dielectric constant $\varepsilon > 1$, then $\varphi_{t_m,p} > \theta_{t_m,p}$ and $\varphi_{r_n,p} > \theta_{r_n,p}$. It follows from (9) that if the wall thickness is over estimated, i.e., $\Delta d > 0$, then $\Delta\tau_{p,mn,d} > 0$. That is, if d_e is greater than the true value d, the applied focusing delays are longer than those required to coherently combine the signal returns for a target at pixel p, i.e., $\tilde{\tau}_{p,mn} > \tau_{p,mn}$. Now, consider a pixel q that is closer to the wall than p, with $\tau_{q,mn} < \tau_{p,mn}$. To image pixel q, where there is no target, under the assumption of wall thickness $d_e > d$, the applied focusing delays are typically greater than those required if there were no wall errors. In this case, $\tilde{\tau}_{q,mn} > \tau_{q,mn}$. The above two time-delay inequalities suggest that there could be a pixel q, where $\tilde{\tau}_{q,mn} \approx \tau_{p,mn}$, rendering a displacement of the target from location p to location q. We note that a pure shift in the target position requires $\tilde{\tau}_{q,mn} = \tau_{p,mn}$, for all values of m and n, otherwise a shift is accompanied with blurriness. The above argument is illustrated in Fig. 4, in which we consider three targets at different positions behind the wall located at (3,30°), (3,−30°), (5,0°). As shown in Fig. 3, the transmit and receive arrays are symmetric about their center point, and are placed against the wall. The transmit array consists of four antennas with inter-element spacing of 0.6 m. The receive array consists of eight antennas with interelement spacing 0.075 m, which is a half-wavelength of a signal with 2-GHz carrier frequency. Both the transmit and receive arrays are located along the x axis at positions listed in Table I. The wall thickness is $d = 0.4$ m, and the dielectric constant is $\varepsilon = 9$, representing a concrete wall. The carrier frequency is 2 GHz, and the pulse bandwidth is 1 GHz. The dielectric constant is assumed known,

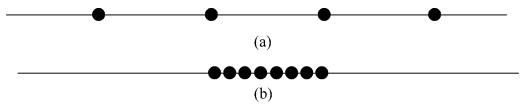

Fig. 3. (a) Transmit array. (b) Receive array.

TABLE I
TRANSMIT AND RECEIVE ARRAY LOCATIONS

Element #	1	2	3	4	5	6	7	8
Transmit (m)	-0.9	-0.3	0.3	0.9				
Receive (m)	-0.2625	-0.1875	-0.1125	-0.0375	0.0375	0.1125	0.1875	0.2625

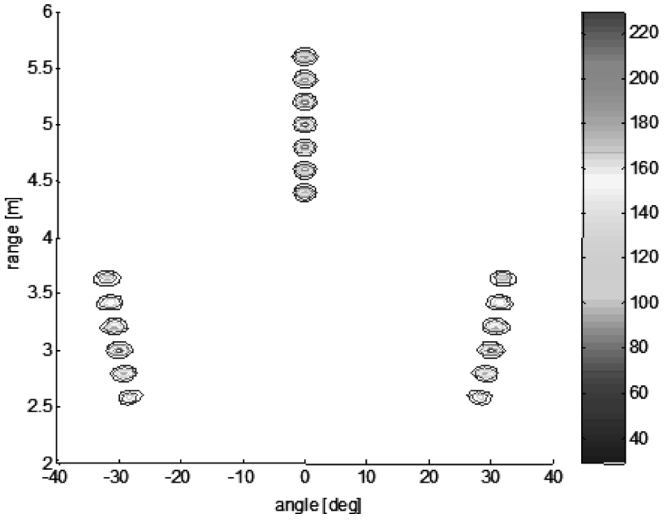

Fig. 4. Shifts in images for different assumed wall thickness values.

i.e., $\varepsilon_e = \varepsilon$, but the wall thickness is unknown and assumed as $d_e = 0.1, 0.2, 0.3, 0.4, 0.5, 0.6$ m. The images corresponding to different pairs of wall parameters (ε, d_e) are generated using (3) and are superimposed. Fig. 4 shows that the targets are clearly shifted away from their true positions. If $\Delta d = d_e - d > 0$, then the target images move toward the array and vise versa. Below, we analyze the effect of the wall thickness errors on target displacement in angle, for an arbitrary standoff distance.

1) Shift of Target in the Image Due to Wall Thickness Error: The mth transmit antenna is located at (x_{t_m}, z_{t_m}), as shown in Fig. 1. In this case, the traveling time, $\tau_{p,m}$, between the mth transmit antenna to the target p, *located at* (x_p, z_p), is expressed as

$$\tau_{p,m} = \frac{z_p - z_{t_m} - d}{c\cos(\varphi_{t_m,p})} + \frac{\sqrt{\varepsilon}d}{c\cos(\varphi_{t_m,p})}. \tag{10}$$

Assume that under the wall error $\Delta d = d_e - d$, the target, whose true position is p at (x_p, z_p), appears at point q at (x_q, z_q). Denote $\Delta x_{pq} = x_q - x_p$ and $\Delta z_{pq} = z_q - z_p$. The relationship between Δx_{pq} and Δz_{pq} is shown in Fig. 5. For a small value of Δd, the estimated time delay from the mth antenna to point q is expressed as

$$\begin{aligned}\tilde{\tau}_{q,m} &= \tau_{p,m} + \Delta\tau_{pq,m} \qquad (11)\\ \Delta\tau_{pq,m} &= \frac{\dot{\partial}\tau_{p,m}}{\partial d}\Delta d + \frac{\partial\tau_{p,m}}{\partial x_q}\Delta x_{pq} + \frac{\partial\tau_{p,m}}{\partial z_q}\Delta z_{pq}\\ &= \frac{\Delta d\sin(\varphi_{t_m,p} - \theta_{t_m,p})}{c\sin(\theta_{t_m,p})} + \frac{\Delta x_{pq}\sin(\varphi_{t_m,p})}{c}\\ &\quad + \frac{\Delta z_{pq}\cos(\varphi_{t_m,p})}{c}. \qquad (12)\end{aligned}$$

Note that $\dot{\partial}\tau_{p,m}/\partial d \triangleq (\sin(\varphi_{t_m,p} - \theta_{t_m,p}))/c\sin(\theta_{t_m,p})$, obtained from (A.8), has considered the subsequent changes of the incident angles due to the change in d. For the array antenna to synthesize an image at position q of a target physically present at location p, the difference between $\tilde{\tau}_{q,m}$ and $\tau_{p,m}$ should ideally be zero for all M antennas. To simplify the problem, we consider small array apertures, and assume the following two conditions to be satisfied at the center of the array (it is not necessary that there physically exists an antenna at the center of the array). First, the time delay $\tilde{\tau}_{q,0}$, where the subscript "0" denotes the center of the array, should be equal to $\tau_{p,0}$,

$$\Delta\tau_{pq,0} = 0. \tag{13}$$

Second, the above time difference is invariant with the position of target p, i.e.,

$$\partial\Delta\tau_{pq,0}/\partial\varphi_{t_0,p} = 0. \tag{14}$$

From (12)

$$\Delta\tau_{pq,0} = \frac{\Delta d}{c}\left[\sqrt{\varepsilon}\cos(\theta_{t_0,p}) - \cos(\varphi_{t_0,p})\right] + \frac{\Delta x_{pq}\sin(\varphi_{t_0,p})}{c} + \frac{\Delta z_{pq}\cos(\varphi_{t_0,p})}{c} \tag{15}$$

where $\theta_{t_0,p}$ and φ_{t_0},p are, respectively, the incident and refraction angles in the wall and the air, related to the path from the center of the transmit array to the target p. Accordingly

$$\frac{\partial\Delta\tau_{pq,0}}{\partial\varphi_{t_0,p}} = \frac{\Delta d}{c}\left(-\frac{\sin(\theta_{t_0,p})\cos(\varphi_{t_0,p})}{\cos(\theta_{t_0,p})} + \sin(\varphi_{t_0,p})\right) + \frac{\Delta x_{pq}\cos(\varphi_{t_0,p})}{c} - \frac{\Delta z_{pq}\sin(\varphi_{t_0,p})}{c}. \tag{16}$$

From (13) and (15)

$$\frac{\Delta d}{c}\left[\sqrt{\varepsilon}\cos(\theta_{t_0,p}) - \cos(\varphi_{t_0,p})\right]\sin(\varphi_{t_0,p}) + \frac{\Delta x_{pq}\sin^2(\varphi_{t_0,p})}{c} + \frac{\Delta z_{pq}\cos(\varphi_{t_0,p})\sin(\varphi_{t_0,p})}{c} = 0. \tag{17}$$

From (14) and (16), we obtain

$$\frac{\Delta d}{c}\left(-\frac{\sin(\theta_{t_0,p})\cos^2(\varphi_{t_0,p})}{\cos(\theta_{t_0,p})} + \sin(\varphi_{t_0,p})\cos(\varphi_{t_0,p})\right) + \frac{\Delta x_{pq}\cos^2(\varphi_{t_0,p})}{c} - \frac{\Delta z_{pq}\sin(\varphi_{t_0,p})\cos(\varphi_{t_0,p})}{c} = 0. \tag{18}$$

Adding (17) to (18)

$$\begin{aligned}\Delta x_{pq} &= -\Delta d\left(\sqrt{\varepsilon}\cos(\theta_{t_0,p})\sin(\varphi_{t_0,p}) - \frac{\sin(\theta_{t_0,p})\cos^2(\varphi_{t_0,p})}{\cos(\theta_{t_0,p})}\right)\\ &= -\Delta d\tan(\theta_{t_0,p})(\varepsilon - 1). \qquad (19)\end{aligned}$$

Similarly, we can obtain

$$\Delta z_{pq} = -\Delta d\left(\frac{\cos(\varphi_{t_0,p})}{\cos(\theta_{t_0,p})}\sqrt{\varepsilon}-1\right). \tag{20}$$

From (19) and (20)

$$\frac{\Delta x_{pq}}{\Delta z_{pq}} = \frac{(\varepsilon-1)\sin(\theta_{t_0,p})}{\cos(\varphi_{t_0,p})\sqrt{\varepsilon}-\cos(\theta_{t_0,p})}. \tag{21}$$

Now, define the function

$$f(\theta) = \frac{\sin(\theta)}{\cos(\varphi)\sqrt{\varepsilon}-\cos(\theta)} \tag{22}$$

with $\sin(\varphi)/\sin(\theta) = \sqrt{\varepsilon}$, $0 \le \theta$, $\varphi < (\pi/2)$. Therefore

$$f'(\theta) = \frac{\cos(\theta)\left(\sqrt{\varepsilon}\cos(\varphi)-\cos(\theta)\right)-\sin\theta\left(\sqrt{\varepsilon}\cos'(\varphi)+\sin(\theta)\right)}{\left(\cos(\varphi)\sqrt{\varepsilon}-\cos(\theta)\right)^2} \tag{23}$$

where

$$\cos'(\varphi) = \frac{d\left(\sqrt{1-\varepsilon\sin^2(\theta)}\right)}{d\theta} = -\frac{\varepsilon\sin(\theta)\cos(\theta)}{\cos(\varphi)}. \tag{24}$$

From (23) and (24)

$$f'(\theta) = \frac{\sqrt{\varepsilon}\cos(\theta)-\cos(\varphi)}{\left(\cos(\varphi)\sqrt{\varepsilon}-\cos(\theta)\right)^2\cos(\varphi)} > 0. \tag{25}$$

The above equation remains valid when the two way traveling time (from transmitter to target and from target to receiver) is considered. When incorporating the effect of both arrays, the shift of the image is given by

$$\Delta x_{pq} = -\Delta d(\varepsilon-1)\left[\tan(\theta_{t_0,p})+\tan(\theta_{r_0,p})\right] \tag{26}$$

$$\Delta z_{pq} = -\Delta d\left(\frac{\cos(\varphi_{t_0,p})}{\cos(\theta_{t_0,p})}\sqrt{\varepsilon}+\frac{\cos(\varphi_{r_0,p})}{\cos(\theta_{r_0,p})}\sqrt{\varepsilon}-2\right) \tag{27}$$

where $\theta_{r_0,p}$ and $\varphi_{r_0,p}$ are, respectively, the incident and refraction angles in the wall and in the air, related to the path from target p to the center of the receive array.

B. Effect of Dielectric Constant Errors

Similar to the wall thickness error, errors in the dielectric constant also impact the imaging quality. However, closed-form expressions similar to (26) and (27) are difficult to obtain due to nonlinearity of the relationship involving dielectric constant errors. If the estimated, or assumed, dielectric constant is $\varepsilon_e = \varepsilon + \Delta\varepsilon$, with known wall thickness, then the corresponding focusing delay for the pixel p becomes

$$\widetilde{\tau}_{p,mn,\varepsilon} = \tau_{p,mn} + \Delta\tau_{p,mn,\varepsilon} \tag{28}$$

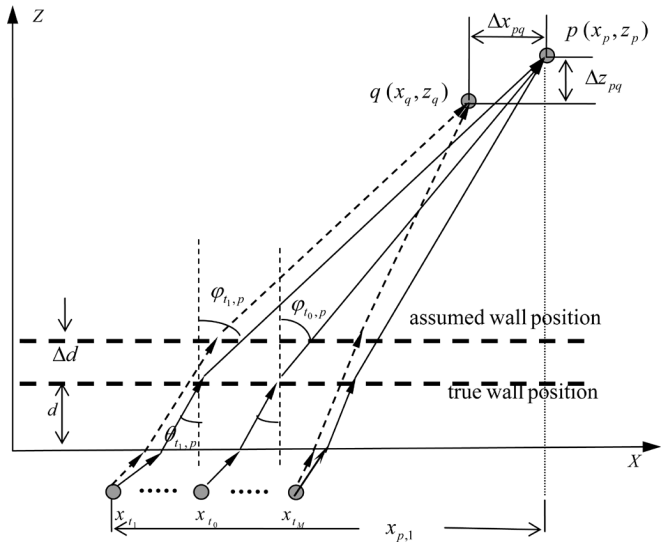

Fig. 5. Geometry for computing the imaged position q corresponding to target p.

where

$$\Delta\tau_{p,mn,\varepsilon} = \frac{d\Delta\varepsilon}{2\sqrt{\varepsilon}c}\left(\frac{1}{\cos(\theta_{t_m,p})}+\frac{1}{\cos(\theta_{r_n,p})}\right). \tag{29}$$

The derivation of (29) is given in Appendix B. It is clear that $\Delta\tau_{p,mn,\varepsilon} > 0$ for $\Delta\varepsilon > 0$. Similar to the case of $d_e > d$, discussed in Section III-A, for $\varepsilon_e > \varepsilon$, the target at location p may be displaced to some pixel q closer to the wall. For illustration, we consider the same wall characteristics and the same three targets as in Section III-A. In this case, however, we assume knowledge of the true wall thickness, $d_e = d$, but we use different values of the wall dielectric constant, $\varepsilon_e = 3.24$, 4.48, 6.25, 9, 12.25, 14.44, 17.64. The images corresponding to different pairs of wall parameters are superimposed in Fig. 6, which shows clear displacement of the targets.

IV. Target Location Estimation Using Two Displacement Trajectories

Consider two standoff distances of the antenna arrays with array centers at $(x_1, -z_1)$, $(x_2, -z_2)$, respectively, with $z_1 < z_2$. The analysis in Section III also applies to this general system placement.

(I) *For target located at* (x_p, z_p) *and* $x_1 = x_2 = x_p$. Let $\theta_{1,p}$ and $\theta_{2,p}$ denote the incident angle relative to the array center, for standoff distance z_1 and z_2, respectively. For the target located at (x_p, z_p), $\theta_{1,p} = \theta_{2,p} = 0$. Equations (19) and (20) state that target p is imaged away from its true position in the z direction if a wall thickness error is introduced. The above argument is verified by the simulation results in Fig. 7. In this simulation, three targets, located at $(3\sin(30^\circ), 3\cos(30^\circ))$, $(-3\sin(30^\circ), 3\cos(30^\circ))$, and (0,5) are imaged from two standoff distances of the radar system, at (0,0) m and (0,−3) m. Dielectric constant $\varepsilon = 9$, and different assumed wall thicknesses, $\Delta d = -0.3$, -0.2, -0.1, 0, 0.1, 0.2, 0.3 m are used. Fig. 7 shows that the image of the target at (0,5) shifts in

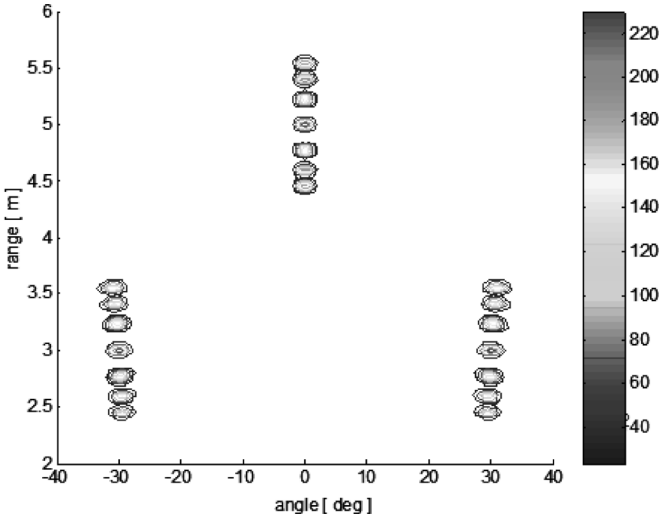

Fig. 6. Shifts in images for different assumed dielectric constant values.

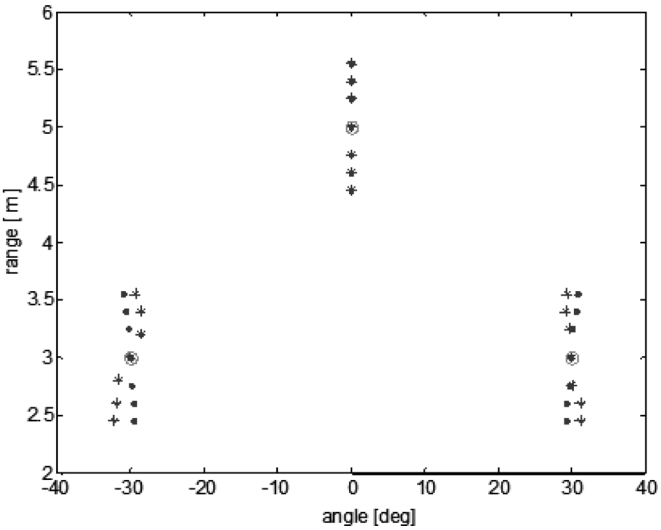

Fig. 8. Peaks of the images in Fig. 7.

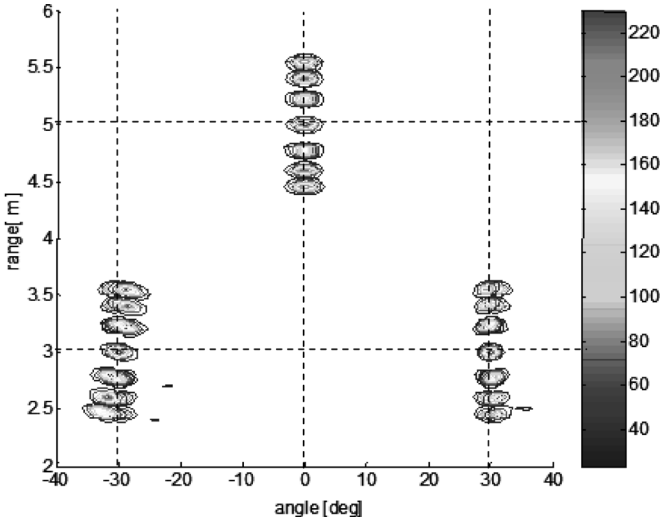

Fig. 7. Image results with two different standoff distances.

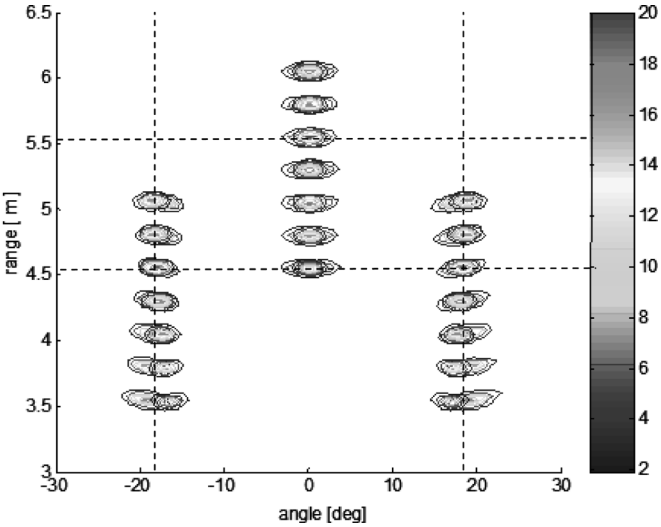

Fig. 9. Images with $\varepsilon_e = 12.25$ from standoff at (0,−3) m and (0,0) m.

range with different assumed wall thickness, but assumes the same position for the two standoff distances.

(II) *For target located at* (x_p, z_p), *with* $\theta_{1,p} > \theta_{2,p} > 0$. Since $\theta_{1,p} > \theta_{2,p} > 0$, then according to (25), the target imaged from the first standoff distance has a different angular shift compared to its image from the second standoff distance. Accordingly, images of the target generated at different standoff distances separate under errors in the wall thickness. The target is, however, imaged at its true position when the true wall thickness is used. Although, for $\Delta_d > 0$, both target images with different standoff distances shift towards the array, the image of the first standoff distance with larger incident angle $\theta_{1,p}$ moves closer to the array than that of the second standoff distance with smaller $\theta_{2,p}$. This is verified by the simulation in Fig. 7. The peaks of the images in Fig. 7 are marked as "." and "*" in Fig. 8, for the two standoff distances. Figs. 7 and 8 demonstrate that the image shift trajectories of the target $(3\sin(30^\circ), 3\cos(30^\circ))$ cross at its true position. As depicted in the same figures, the above argument also applies to the other noncenter target. Similar behavior of target images and trajectories is exhibited for the case in which the dielectric constant is assumed.

We consider next the general case, where both the wall thickness and dielectric constant are unknown. The two system standoff distances at (0,0) and (0,−3) is used to image three targets located at $(4.5\sin(18^\circ), 4.5\cos(18^\circ))$ m, $(4.5\sin(-18^\circ), \cos(-18^\circ))$ m, and (0,5.5) m. The wall parameters are $d = 0.4$ m, $\varepsilon = 9$. The simulation result is presented in Fig. 9 with assumed dielectric constant $\varepsilon_e = 12.25 \neq \varepsilon$, and seven assumed wall thickness values $d_e = 0.1$, 0.2, 0.3, 0.4, 0.5, 0.6, 0.7 m. The figure shows that the image trajectories from the two standoff distances of each side target intersect approximately at the true wall thickness value.

V. Alternative Imaging Approach

The analysis in the previous section shows that the intersection of the target image trajectories for two standoff distances provides good estimates of the wall parameters, yielding correct

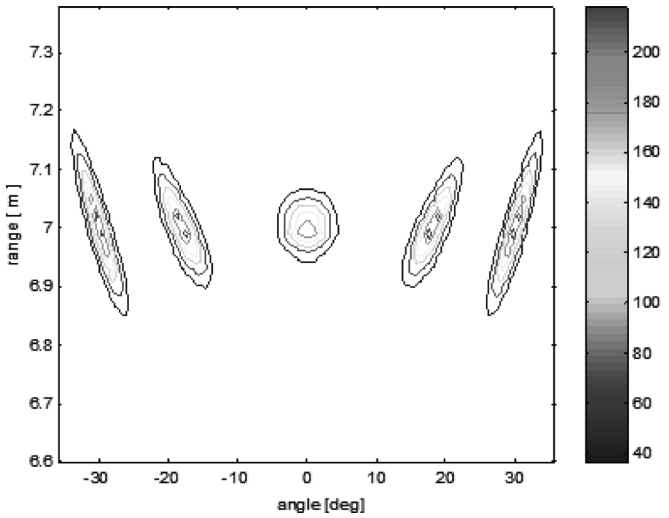

Fig. 10. Image with standoff distance 8 m.

target locations. The trajectory is formed by tracing the target image peaks. This approach works well for smaller standoff distances. However, there are potential problems in adopting this approach for longer standoff distances.

A. Problem in Tracking Image Peaks

It is important to note that in order to find the intersection of the target displacement trajectories with two different standoff distances, the coordinate systems must not be changed for different array positions. For each standoff distance, the imaged region is divided into small image pixels with the same range and angle coordinate system. Suppose the center of the imaging system at one standoff distance is chosen as the origin of the coordinate system. Using the same coordinates, the images obtained at a longer standoff distance will have a lower angle resolution. Furthermore, the pixels in the same range cell corresponding to one standoff distance may not have the same time delay to the center of array when imaged from another standoff distance. Therefore, a target, especially one with a long distance from antenna array, might be imaged in several image pixels that extend over several angle and range cells. This argument is verified by the simulation result in Fig. 10. We consider five targets located at (7,30°), (7,18°), (7,0°), (7,−18°), (7,−30°). The exact values of wall thickness and dielectric constant are 0.4 m and 9, respectively. The transmit and receive antenna arrays have the structure depicted in the Table I, with standoff distance 8 m.

Theoretically, the peak position of target image is in the center of the target image. However, the image is obtained by the discrete sampling of image pixels in range and angle. Therefore, the sample points might not be exactly in the center of the target image. Tracing the target shifts of low resolution images could cause problems for the target location estimation schemes that incorporate target trajectory intersections.

B. New Approach for Imaging Using Different Array Placements

From the analysis in Section IV, the target images generated from different standoff distances coincide or highly overlap at the target true position, when the true wall parameters are used. When an incorrect wall thickness is applied, the target is imaged in different positions from the two standoff distances, i.e., it will appear separated in a superimposed image. Therefore, one approach to estimate the true position of a target is to form the composite images with different assumed wall thickness values and find the wall characteristics at which the images of the target from different standoff distances are mostly overlapping. The latter can be accomplished using a focusing or sharpness metric. In the following, we give a pseudocode of the proposed target location estimation algorithm with known dielectric constant ε.

1) Generate a sequence of images $A_{d_{e1}}, A_{d_{e2}}, \cdots, A_{d_{eK}}$, for a given array standoff distance and using ε. These images correspond to the assumed wall thickness values $d_{e_1}, d_{e_2}, \cdots, d_{eK}$.
2) Repeat step 1) and generate another sequence of images $B_{d_{e1}}, B_{d_{e2}}, \cdots, B_{d_{eK}}$, for another standoff distance.
3) Generate a composed image $I_{d_{e1}}, I_{d_{e2}}, \cdots, I_{d_{eK}}$ from $A_{d_{e1}}, A_{d_{e2}}, \cdots, A_{d_{eK}}$ and $B_{d_{e1}}, B_{d_{e2}}, \cdots, B_{d_{eK}}$, with $I_{d_{ek}} = A_{d_{ek}} + B_{d_{ek}}, k = 1, \ldots, K$. $I_{d_{e1}}, I_{d_{e2}}, \cdots, I_{d_{eK}}$ is a new and composite image sequence over the assumed wall thickness variable.
4) Find the optimum wall thickness d_{ek_0} at which the applied focusing criterion assumes the largest or the smallest value for the image sequence $I_{d_{e1}}, I_{d_{e2}}, \cdots, I_{d_{eK}}$. If multiple answers exist, then select the one that is more physically acceptable.
5) A more accurate estimate of the wall thickness can be obtained if more images $A_{d_{e1}}, A_{d_{e2}}, \cdots, A_{d_{eK}}$ and $B_{d_{e1}}, B_{d_{e2}}, \cdots, B_{d_{eK}}$ are generated and added around the initial estimate, d_{ek_0}.
6) Use the wall parameter (ε, d_{ek_0}) to generate the final image.

There are different criteria that can be used in step 4) to measure the image focusing levels. One of the most commonly used focusing criterion is the minimum entropy [19], [20]. For each composite target image $I_{d_{ei}}$ in the target image sequence $I_{d_{e1}}, I_{d_{e2}}, \cdots, I_{d_{eK}}$, we calculate the entropy $E(d_{ei})$ of $I_{d_{ei}}$, as

$$E(d_{ei}) = -\sum_{l=1}^{L}\sum_{j=1}^{J} p_{l,j}(d_{ei}) \log\left(p_{l,j}(d_{ei})\right), \qquad p_{l,j}(d_{ei}) = \left|x_{d_{ei}}(l,j)\right|^2. \quad (30)$$

where $p_{l,j}(d_{ei})$ is the square of the pixel value $x_{d_{ei}}(l,j)$ of $I_{d_{ei}}$, and L and J are the range and cross-range sizes of image $I_{d_{ei}}$, respectively. The parameter $\hat{d}_e$, corresponding to the smallest value of $E(d_{ei})$, is taken as the estimate of the wall thickness. The motivation of using the minimum entropy of the composite image to measure the degree of overlapping of images $A_{d_{ei}}$ and $B_{d_{ei}}$ is that the more $A_{d_{ei}}$ and $B_{d_{ei}}$ overlap, the larger the change in the image pixel values. The above criterion is typically applied in synthetic aperture radar (SAR) motion compensation and autofocus [19], [20]. We note that there are other equally effective criteria [21]–[24] that can also be used in (30).

For illustration, consider the original transmit and receive antenna structures of Table I. The imaging system is positioned at (−3, −4) m and (1, −8) m, respectively. We consider three targets behind the wall, located at (0,7) m,

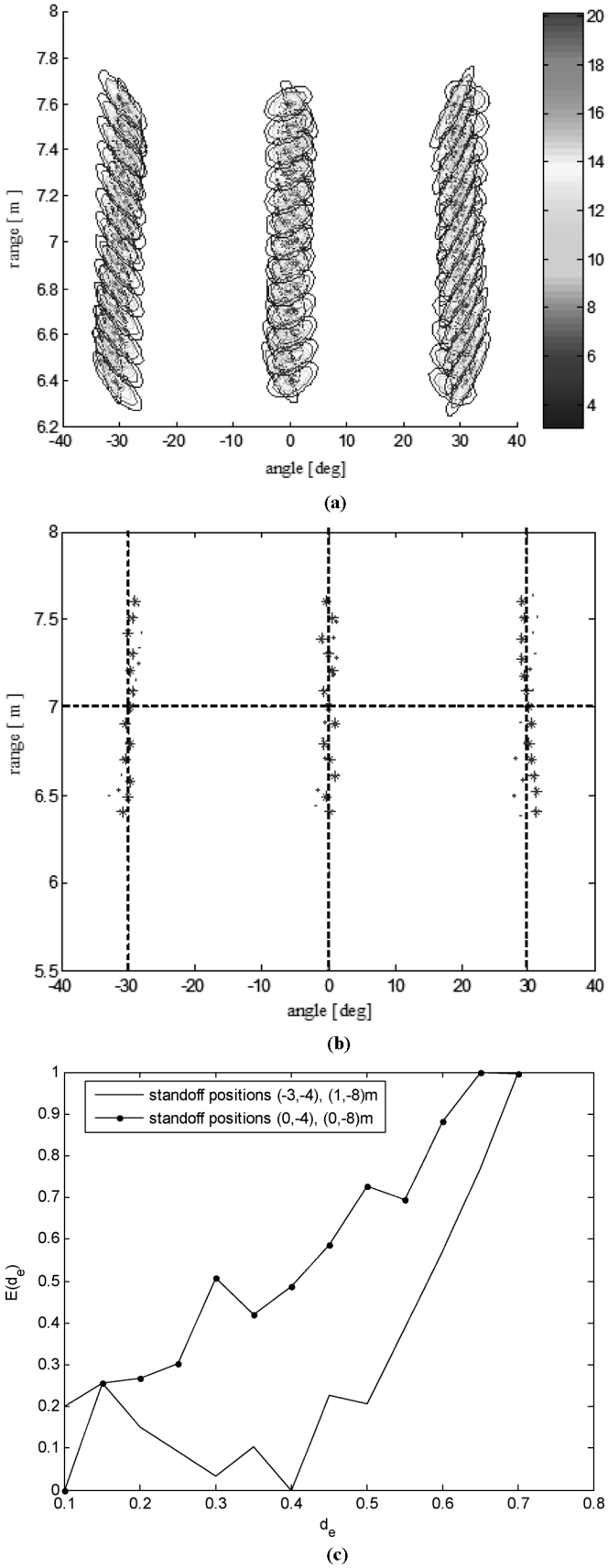

Fig. 11, (a) Images with $\varepsilon_e = \varepsilon = 9$ from two standoff distances $(-3, -4)$ m, and $(1, -8)$ m. (b) Peaks of the images in Fig. 11(a). (c) Normalized entropies of composite images.

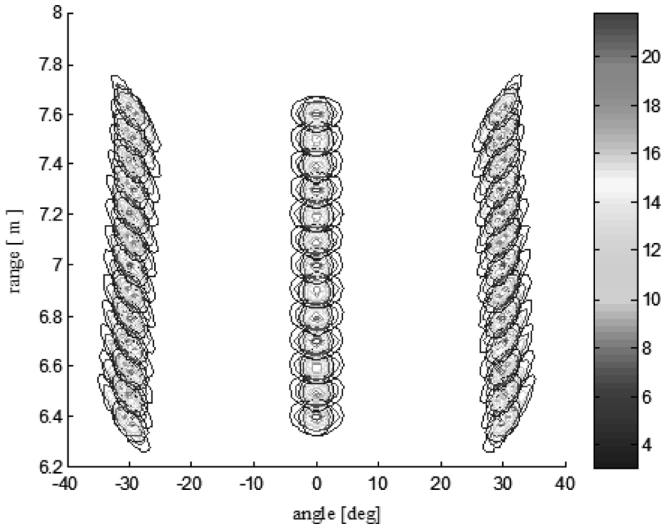

Fig. 12. Images with $\varepsilon_e = \varepsilon = 9$ from two standoff distances (0, -4) m, and (0, -8) m.

$(7\sin(30^\circ), 7\cos(30^\circ))$ m, and $(-7\sin(30^\circ), 7\cos(30^\circ))$ m. The true wall parameters are $d = 0.4$ m, $\varepsilon = 9$. In the simulation, the dielectric constant is known. For each array placement, the wall thickness values $d_e = 0.1$, 0.15, 0.2, 0.25, 0.30, 35, 0.4, 0.45, 0.55, 0.6, 65, 0.7 m are assumed. Superimposed images from the two standoff distances are shown in Fig. 11(a), and the corresponding peaks of the images are shown in Fig. 11(b). Fig. 11(b) shows that, due to large target image dispersions over neighboring pixels, the target trajectories cannot be properly formed. Therefore, we resort to using a focusing metric to solve the problem. The entropy of the composite image in Fig. 11(a) is computed and plotted with the solid line in Fig. 11(c) with respect to the assumed wall thickness. It shows a minimum value at $d_e = d = 0.4$ m. The above algorithm can also be applied to estimate the dielectric constant when the wall thickness is unknown.

In the next example, we examine the sensitivity of the proposed techniques to the imaging system placements. Fig. 12 shows a simulation result for the targets of Fig. 11, but the two standoff positions (0, -4) m and (0, -8) m are used instead of $(-3, -4)$ m and $(1, -8)$ m in Fig. 11. Fig. 12 shows the target images with different assumed wall thickness. The incident angles from the standoff positions in Fig. 12 are smaller than those in Fig. 11, causing the images to overlap, while they are separated in Fig. 11. The entropy of the composite images for Fig. 12 (a) is plotted with the ".$-$" line in Fig. 11(c). It does not reach a minimum at the true value $d = 0.4$ m of wall thickness. Similar behavior is observed when the system is shifted parallel to the wall without changing the standoff distance.

C. Imaging With Both Parameters Unknown

Now, we consider the case in which both the wall thickness and the dielectric constant are unknown. We first assume a value of one of the two parameters, say the dielectric constant, ε_e. Then, we proceed with the same steps used in Section V-B, where the dielectric constant is known. That is, we generate a

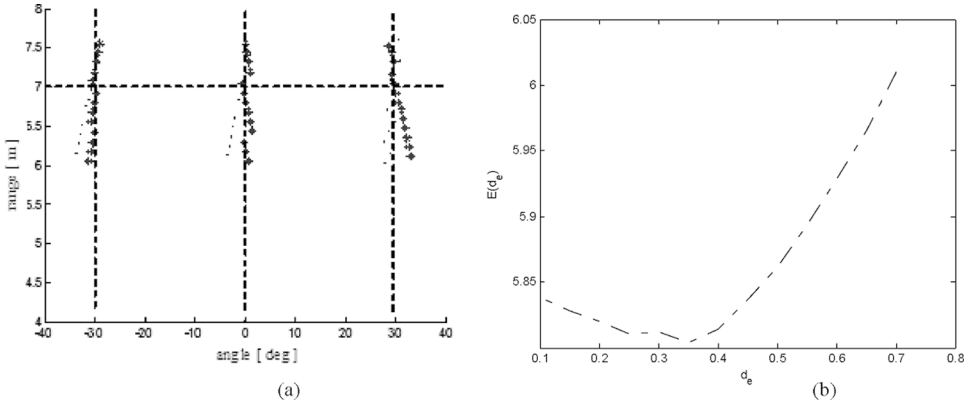

Fig. 13. Peaks and entropy of the composite image with $\varepsilon_e = \varepsilon = 12.25$ from two standoff distances $(-3, -4)$ m, and $(1, -8)$ m.

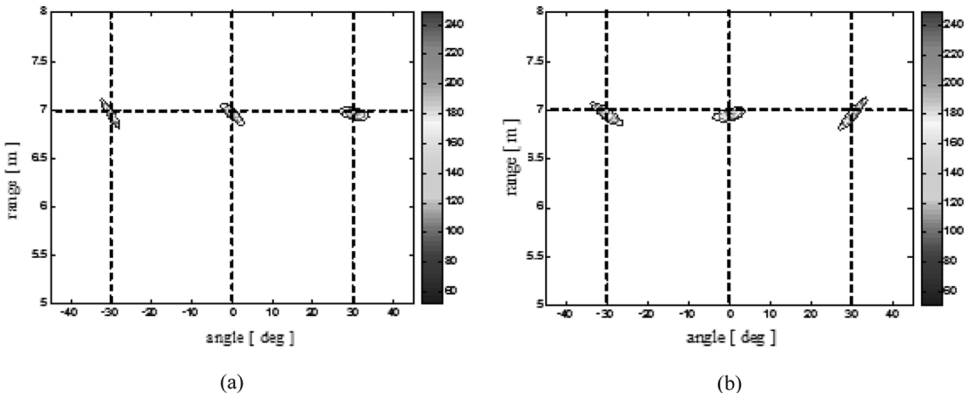

Fig. 14. Final image from single standoff with $(d_e, \varepsilon_e) = (0.35, 12.25) \neq (d, \varepsilon)$. (a) Standoff at $(-3, -4)$ m; (b) standoff at $(1, -8)$ m.

sequence of images using different assumed values of the wall thickness. The trajectories of target displacements with different standoff distances cross at some assumed wall thickness d_{ε_e}. Notice that the estimated d_{ek_0} in this case depends on the assumed dielectric constant, ε_e. Therefore, the pair $(\varepsilon_e, d_{ek_0})$ employed to generate the final image is not unique.

Consider the two standoff positions of the imaging system, and the true wall parameters to be the same as those in Fig. 11. We assume the wall dielectric constant to be $\varepsilon_e = 12.25$. For each one of the array position, the wall thickness values $d_e =$ 0.1, 0.15, 0.2, 0.25, 0.30, 35, 0.4, 0.45, 0.55, 0.6, 65, 0.7 m are assumed. Superimposed images from the two standoff distances are generated and the corresponding peaks of the images are shown in Fig. 13(a). Similar to Fig. 11(b), the target trajectories cannot be properly formed by tracing the highest peaks of the images and the intersection points are not clear. Therefore, we resort to using a focusing metric to solve the problem. The entropy of composite image for each wall pair is computed and plotted in Fig. 13(b) with respect to the assumed wall thickness. The entropy assumes a minimum value at $d_e = 0.35$ m, which differs from the true wall thickness value. However, the wall parameter pair $(d_e, \varepsilon_e) = (0.35, 12.25) \neq (d, \varepsilon)$ yields correct target positions for both standoff distances. This is because the effects of the errors in both d and ε are canceled out, leading to the correct set of delays required to coherently combine the waveform returns from the target positions. The imaging results for 4 m and 8 m standoff distances are shown in Fig. 14(a) and (b), respectively.

VI. Conclusion

"Seeing" through the wall using radio frequencies is an emerging technology that is currently sought out by both the commercial and government sectors. For logistical and safety reasons, imaging is preferably performed at a standoff distance from the external wall. This requirement, combined with the fact that wall characteristics may be unknown, presents a challenge in producing accurate and reliable images. In this paper, we proposed a wideband beamforming-based technique that allows the system operator to perform imaging with wall parameter ambiguities and from a standoff distance. The approach depends on the assumption that imaging can be obtained at two or multiple standoff distances. We focused on point targets and assume single uniform walls. The approach traces the images as they shift in position for different assumed wall thickness and dielectric constant. The target image trajectories for two standoff distances intersect. The wall parameters corresponding to the intersection point are used to provide the target positions. The paper presented an alternative approach that is useful at long standoff distances and incorporates both the shift and blurriness effects of the target when using incorrect wall parameters. The entropy minimization approach was applied to the composite images from two standoff distances to determine

the target position with least blurriness. Several simulation examples were presented which demonstrated the effectiveness of the proposed approach. This paper has only dealt with two-dimensional imaging using one-dimensional array. The applicability of the proposed techniques to three-dimensional (3-D) imaging is expected to hold but should be separately analyzed and verified.

APPENDIX A

For simplicity, we only consider the traveling time from a transmit antenna to the target. As shown in Fig. 5, without errors in the wall thickness estimation

$$x_{p,m} = x_p - x_{tm} = d\tan(\theta_{t_m,p}) + h\tan(\varphi_{t_m,p}) \quad \text{(A.1)}$$

where $h = h_1 = h_2 = z_p - z_{t_m} - d$. We consider the traveling time when there is an error $\Delta d = d_e - d$ in the estimated wall thickness. When d changes to $d+\Delta d$ (and subsequently h changes to $h-\Delta d$) and $\varphi_{t_m,p}$ changes to $\varphi_{t_m,p}+\Delta\varphi_{t_m,p}$ (and subsequently $\theta_{t_m,p}$ changes to $\theta_{t_m,p}+\Delta\theta_{t_m,p}$), the change in $x_{p,m}$ can be approximated by

$$\begin{aligned}\Delta x_{p,m} &= \frac{\partial x_{p,m}}{\partial d}\Delta d + \frac{\partial x_{p,m}}{\partial h}\Delta h + \frac{\partial x_{p,m}}{\partial \theta_{t_m,p}}\Delta\theta_{t_m,p} \\ &\quad + \frac{\partial x_{p,m}}{\partial \varphi_{t_m,p}}\Delta\varphi_{t_m,p} \\ &= \tan(\theta_{t_m,p})\,\Delta d + \tan(\varphi_{t_m,p})\,\Delta h \\ &\quad + d\cos^{-2}(\theta_{t_m,p})\,\Delta\theta_{t_m,p} \\ &\quad + h\cos^{-2}(\varphi_{t_m,p})\,\Delta\varphi_{t_m,p}. \end{aligned} \quad \text{(A.2)}$$

For the path to pass through the true target position, $\Delta x_{p,m} = 0$. That is

$$\Delta d\tan(\theta_{t_m,p}) + \Delta h\tan(\varphi_{t_m,p}) + d\cos^{-2}(\theta_{t_m,p})\,\Delta\theta_{t_m,p} + h\cos^{-2}(\varphi_{t_m,p})\,\Delta\varphi_{t_m,p} = 0. \quad \text{(A.3)}$$

From the Snell's law, $\sin(\varphi_{t_m,p}) = \sqrt{\varepsilon}\sin(\theta_{t_m,p})$, we can deduce the approximation

$$\Delta\theta_{t_m,p} = \Delta\varphi_{t_m,p}\frac{\cos(\varphi_{t_m,p})}{\sqrt{\varepsilon}\cos(\theta_{t_m,p})}. \quad \text{(A.4)}$$

Substituting (A.4) in (A.3) yields

$$\Delta d\tan(\theta_{t_m,p}) + \Delta h\tan(\varphi_{t_m,p}) + \frac{d}{\sqrt{\varepsilon}}\cos^{-3}(\theta_{t_m,p})\times\cos(\varphi_{t_m,p})\,\Delta\varphi_{t_m,p} + h\cos^{-2}(\varphi_{t_m,p})\,\Delta\varphi_{t_m,p} = 0. \quad \text{(A.5)}$$

Since $\Delta h = -\Delta d$, then

$$\Delta\varphi_{t_m,p} = \frac{\Delta d[\tan(\varphi_{t_m,p}) - \tan(\theta_{t_m,p})]}{\frac{d}{\sqrt{\varepsilon}}\frac{\cos(\varphi_{t_m,p})}{\cos^3(\theta_{t_m,p})} + \frac{h}{\cos^2(\varphi_{t_m,p})}}. \quad \text{(A.6)}$$

Equation (A.6) shows the necessary shift of the incident angles for the path traveling from the mth antenna to the point p when the wall thickness error is taken into account. On the other hand, the total travel time from the mth antenna to the target position p is given by

$$\tau_{p,m} = \frac{1}{c}\left(\frac{\sqrt{\varepsilon}d}{\cos(\theta_{t_m,p})} + \frac{h}{\cos(\theta_{t_m,p})}\right). \quad \text{(A.7)}$$

Therefore, the additional travel time due to Δd and $\Delta\varphi_{t_m,p}$ can be expressed using first-order approximation as

$$\begin{aligned}\Delta\tau_{p,m} &= \frac{\partial\tau_{p,m}}{\partial d}\Delta d + \frac{\partial\tau_{p,m}}{\partial\theta_{t_m,p}}\Delta\theta_{t_m,p} + \frac{\partial\tau_{p,m}}{\partial\varphi_{t_m,p}}\Delta\varphi_{t_m,p} \\ &= \frac{\partial\tau_{p,m}}{\partial d}\Delta d + \Delta\varphi_{t_m,p} \\ &\quad \times\left(\frac{\partial\tau_{p,m}}{\partial\theta_{t_m,p}}\frac{\cos(\varphi_{t_m,p})}{\sqrt{\varepsilon}\cos(\theta_{t_m,p})} + \frac{\partial\tau_{p,m}}{\partial\varphi_{t_m,p}}\right) \\ &= \frac{\Delta d}{c}\left(\frac{\sqrt{\varepsilon}}{\cos(\theta_{t_m,p})} - \frac{1}{\cos(\varphi_{t_m,p})}\right) \\ &\quad + \frac{\Delta\varphi_{t_m,p}}{c}\left(\frac{d\cos(\varphi_{t_m,p})}{\cos^2(\theta_{t_m,p})}\tan(\theta_{t_m,p}) + \frac{h}{\cos(\varphi_{t_m,p})}\tan(\varphi_{t_m,p})\right) \\ &= \frac{\Delta d}{c}\left(\frac{\sqrt{\varepsilon}}{\cos(\theta_{t_m,p})} - \frac{1}{\cos(\varphi_{t_m,p})}\right) \\ &\quad + \frac{\Delta d}{c}[\tan(\varphi_{t_m,p}) - \tan(\theta_{t_m,p})]\sin(\varphi_{t_m,p}) \\ &= \frac{\Delta d}{c}\left[\sqrt{\varepsilon}\cos(\theta_{t_m,p}) - \cos(\varphi_{t_m,p})\right] \\ &= \frac{\Delta d}{c}\frac{\sin(\varphi_{t_m,p} - \theta_{t_m,p})}{\sin(\theta_{t_m,p})}. \end{aligned} \quad \text{(A.8)}$$

APPENDIX B

We consider the situation where there is an error in the estimated value of the dielectric constant of the wall material, $\Delta\varepsilon = \varepsilon_e - \varepsilon$. The incident angles are adjusted so that the new path links the mth antenna and the target point, p. From (A.1), we obtain the following first-order approximation:

$$\begin{aligned}\Delta x_{p,m} &= \frac{\partial x_{p,m}}{\partial\theta_{t_m,p}}\Delta\theta_{t_m,p} + \frac{\partial x_{p,m}}{\partial\varphi_{t_m,p}}\Delta\varphi_{t_m,p} \\ &= \frac{\Delta\theta_{t_m,p}d}{\cos^2(\theta_{t_m,p})} + \frac{\Delta\varphi_{t_m,p}d}{\cos^2(\varphi_{t_m,p})}. \end{aligned} \quad \text{(B.1)}$$

For the path to pass through the true target position, $\Delta x_{p,m} = 0$. That is

$$\frac{\Delta\theta_{t_m,p}d}{\cos^2(\theta_{t_m,p})} + \frac{\Delta\varphi_{t_m,p}d}{\cos^2(\varphi_{t_m,p})} = 0. \quad \text{(B.2)}$$

From (A.8), the additional time due to the error $\Delta\varepsilon$ becomes

$$\begin{aligned}\Delta\tau_{p,m} &= \frac{\partial\tau_{p,m}}{\partial\varepsilon}\Delta\varepsilon + \frac{\partial\tau_{p,m}}{\partial\theta_{t_m,p}}\Delta\theta_{t_m,p} + \frac{\partial\tau_{p,m}}{\partial\phi_{p,m}}\Delta\varphi_{t_m,p} \\ &= \frac{1}{c}\left(\frac{\Delta\varepsilon}{2\sqrt{\varepsilon}}\frac{d}{\cos(\theta_{t_m,p})} + \frac{\sqrt{\varepsilon}d\sin(\theta_{t_m,p})}{\cos^2(\theta_{t_m,p})}\Delta\theta_{t_m,p} + \frac{h\sin(\varphi_{t_m,p})}{\cos^2(\varphi_{t_m,p})}\Delta\varphi_{t_m,p}\right) \\ &= \frac{\Delta\varepsilon}{2c\sqrt{\varepsilon}}\frac{d}{\cos(\theta_{t_m,p})}. \end{aligned} \quad \text{(B.3)}$$

ACKNOWLEDGMENT

The authors would like to thank Dr. Fauzia Ahmad at the Center for Advanced Communications, Villanova University, Villanova, PA, for her valuable input and discussion on the subject.

REFERENCES

[1] D. D. Ferris, Jr., and N. C. Currie, "A survey of current technologies for through-the-wall surveillance (TWS)," in *Proc. SPIE*, Boston, MA, Nov. 1998, vol. 3577, Sensors, C3I, Infor. and Training Techn. for Law Enforcement, pp. 62–72.

[2] S. Nag, H. Fluhler, and M. Barnes, "Preliminary interferometric images of moving targets obtained using a time-modulated ultra-wide band through-wall penetration radar," in *Proc. IEEE Radar Conf.*, Atlanta, GA, May 2001, pp. 64–69.

[3] N. C. Wild *et al.*, "Ultrasonic through-the wall surveillance system," in *Proc. SPIE*, Boston, MA, Nov. 2000, vol. 4232, Enabling Techn. for Law Enforcement and Security, pp. 167–176.

[4] E. F. Greneker, "RADAR flashlight for through-the-wall detection of humans," in *Proc. SPIE*, Orlando, FL, Apr. 1998, vol. 3375, Targets and Backgrounds: Characterization and Representation IV, pp. 280–285.

[5] J. D. Black, "Motion and ranging sensor through-the-wall surveillance system," in *Proc. SPIE*, Orlando, FL, Apr. 2002, vol. 4708, Sensors and C3I Techn. for Homeland Defense and Law Enforcement, pp. 114–121.

[6] A. R. Hunt, "Stepped-frequency CW radar for concealed weapon detection and through-the-wall surveillance," in *Proc. SPIE*, Orlando, FL, Apr. 2002, vol. 4708, Sensors and C3I Techn. for Homeland Defense and Law Enforcement, pp. 99–105.

[7] S. Nag *et al.*, "An ultra-wideband through-the-wall radar for detecting the motion of people in real time," in *Proc. SPIE*, Orlando, FL, Apr. 2002, vol. 4744, Radar Sensor Technology and Data Visulization, pp. 48–57.

[8] D. G. Falconer, R. W. Ficklin, and K. G. Konolige, "Detection, location, and identification of building occupants using a robot-mounted through-wall radar," in *Proc. SPIE*, Orlando, FL, Apr. 2000, vol. 4037, Battlefield Biomedical Technology II, pp. 72–81.

[9] F. Ahmad, M. G. Amin, and S. A. Kassam, "Synthetic aperture beamformer for imaging through a dielectric wall," *IEEE Trans. Aerosp. Electron. Syst.*, vol. 41, no. 1, pp. 271–283, Jan. 2005.

[10] W. Choi and T. Sarkar, "Echo cancellation using a homomorphic deconvolution," presented at the IEEE AP-S Int. Symp. USNC/URSI Nat. Radio Science Meeting, Monterey, CA, Jun. 2004.

[11] A. R. Hunt, "Image formation through walls using a distributed radar sensor network," presented at the IEEE AP-S Int. Symp. USNC/URSI Na. Radio Science Meeting, Monterey, CA, Jun. 2004.

[12] P. Withington, H. Fluhler, and S. Nag, "Enhancing homeland security with advanced UWB sensors," *IEEE Microw. Mag.*, vol. 4, no. 3, pp. 51–58, Sep. 2003.

[13] C. Chen, K. Yao, and R. E. Hudson, "Source localization and beamforming," *IEEE Signal Process. Mag.*, pp. 30–39, May 2002.

[14] V. Murino, C. Regazzoni, A. Trucco, and G. Vernazza, "A noncoherent correlation technique and focused beamforming for ultrasonic underwater imaging: A comparative analysis," *IEEE Trans. Ultrason., Ferroelectr., Freq. Control*, vol. 41, no. 5, pp. 621–630, Sep. 1994.

[15] D. G. Falconer, K. N. Steadman, and D. G. Watters, "Through-the wall differential radar," in *Proc. SPIE*, Boston, MA, Nov. 1996, vol. 2938, Enabling Technologies for Law Enforcement, pp. 147–151.

[16] D. E. Manolakis, "Efficient solution and performance analysis of 3-D position estimation by trilateration," *IEEE Trans. Aerosp. Electron. Syst.*, vol. 32, no. 4, pp. 1239–1248, Oct. 1996.

[17] F. Ahmad and M. G. Amin, "A noncoherent radar system approach for through-the-wall imaging," in *Proc. SPIE*, Bellingham, WA, Mar. –April 2005, vol. 5778, Sensor, and Command, Control, Communications, and Intelligence Technologies for Homeland Security and Homeland Deffense IV.

[18] G. Wang and M. G. Amin, "A new approach for target locations in the presence of wall ambiguities," presented at the IEEE Symp. Signal Processing Information Technology (ISSPIT'04), Rome, Italy, Dec. 2004.

[19] G. Wang and Z. Bao, "The minimum entropy criterion of range alignment in ISAR motion compensation," in *Proc. Int. Radar Conf. (Radar'97)*, Edinburgh, UK, Oct. 1997, pp. 236–239.

[20] M. Soumekh, "Auto-focusing of wide-bandwidth and wide-beamwidth SAR imagery," presented at the Int. Conf. Image Processing (ICIP'05), Genova, Italy, Sep. 2005.

[21] L. Ta-Hsin and L. Ke-Shin, "Deblurring two-tone images by a joint estimation approach using higher-order statistics," in *Proceedings of the IEEE Signal Processing Workshop on Higher-Order Statistics*, Banff, Canada, Jul. 1997.

[22] L. Alparone, F. Argenti, B. Aiazzi, and S. Baronti, "Multiresolution approaches to adaptive speckle reduction in synthetic aperture radar images," presented at the Int. Conf. Image Processing (ICIP), Barcelona, Spain, Sep. 2003.

[23] S. Fortune, M. Hayes, and P. Gough, "Statistical autofocus of synthetic aperture sonar images using image contrast optimization," in *Proc. MTS/IEEE Conf. Exhibition OCEANS 2001*, Honolulu, HI, Nov. 2001, vol. 1, pp. 163–169.

[24] G. Mandapati and M. Amin, "Blurness and focusing-defocusing for through the wall radar imaging with wall ambiguities," presented at the IEEE Symp. Signal Processing Information Technology (ISSPIT), Rome, Italy, Dec. 2004.

Genyuan Wang (M'01) received the B.Sc. and M.S. degrees in mathematics from Shaanxi Normal University, Xi'an, China, in 1985 and 1988, respectively, and the Ph.D. degree in electrical engineering from Xidian University, Xi'an China, in 1998.

From 1988 to 1994, he worked at Shaanxi Normal University as an Assistant Professor and then an Associate Professor. From 1994 to 1998, he worked at Xidian University as a Research Assistant. He worked with Department of Electrical and Computer Engineering, University of Delaware, as a Postdoctoral Fellow. Currently, he works as a Research Associate with Center of Advanced Communications, Villanova University, Villanova, PA. His research interests are radar imaging, radar signal processing, adaptive filters, OFDM systems, channel equalization, channel coding, space–time coding, and multiple-input multiple-output for broadband wireless communication systems.

Moeness G. Amin (S'82–M'83–SM'91–F'01) received the Ph.D. degree from the University of Colorado, Boulder, in 1984.

He has been on the Faculty of Villanova University, Villanova, PA, since 1985, where is now a Professor in the Department of Electrical and Computer Engineering and the Director of the Center for Advanced Communications. He has over 300 publications in the areas of wireless communications, time-frequency analysis, smart antennas, interference cancellation in broadband communication platforms, radar imaging, direction finding, over-the-horizon radar, and channel equalizations.

Dr. Amin is the recipient of the IEEE Third Millennium Medal; Distinguished Lecturer of the IEEE Signal Processing Society for 2003; Member of the Franklin Institute Committee on Science and the Arts; Recipient of the 1997 Villanova University Outstanding Faculty Research Award; and Recipient of the 1997 IEEE Philadelphia Section Service Award. He was the Technical Chair of the Second IEEE International Symposium on Signal Processing and Information Technology, Morocco, 2002; The General and Organization Chair of the IEEE Workshop on Statistical Signal and Array Processing, Pennsylvania, 2000; The General and Organization Chair of the IEEE International Symposium on Time-Frequency and Time-Scale Analysis, Pennsylvania, 1994. He was an Associate Editor of the IEEE TRANSACTIONS ON SIGNAL PROCESSING from 1996 to 1998. He was a member of the IEEE Signal Processing Society Technical Committee on Signal Processing for Communications from 1998 to 2002 and was a Member of the IEEE Signal Processing Society Technical Committee on Statistical Signal and Array Processing from 1995 to 1997.